Applied Surface Science 583 (2022) 152441

Contents lists available at ScienceDirect

Applied Surface Science

journal homepage: www.elsevier.com/locate/apsusc

Full Length Article

TiO_2 encrusted MXene as a High-Performance anode material for Li-ion batteries

Hanan Abdurehman Tariq [a], Umair Nisar [a,*], Jeffin James Abraham [a], Zubair Ahmad [b], Siham AlQaradawi [c], Ramazan Kahraman [d], R.A. Shakoor [a,*]

[a] Center for Advanced Materials (CAM), Qatar University, Doha P. O. Box 2713, Qatar
[b] Young Scientist Center (YSC), Qatar University, Doha P. O. Box 2713, Qatar
[c] Department of Chemistry & Earth Sciences, College of Arts and Science, Qatar University, Doha P. O. Box 2713, Qatar
[d] Dept. of Chemical Engineering, College of Engineering, Qatar University, Doha P. O. Box 2713, Qatar

ARTICLE INFO

Keywords:
Li-ion battery
Anode
MXene
TiO_2
Kinetics
Cyclability
Rate capability
Ti3C

ABSTRACT

TiO_2 has the potential to be a viable anode material for high-power lithium-ion batteries (LIBs). However, the lower electronic conductivity of TiO_2 limits its practical applications. Here, the synthesis of novel TiO_2 decorated Ti_3C-MXene anode for LIBs using in-situ hydrolysis is discussed. MXenes are well known for their outstanding structural stability and superior electronic conductivities; thus, using MXenes as a host material for TiO_2 may improve its structural and electrical characteristics. Scanning and transmission electron microscopy (SEM & TEM) examination revealed that the in-situ method resulted in a uniform and comformal coating of TiO_2 (27.5 nm) on the inner and outer surfaces of MXene surfaces. BET analysis revealed that the larger surface area of MXene-TiO_2 nanocomposite enhanced the active sites for lithium intercalation, which improved electrochemical performance. Furthermore, electrochemical impedance spectroscopy (EIS) analysis revealed faster kinetics for MXene-TiO_2 materials when compared to the TiO_2 anode. Compared to pristine TiO_2 anode, 5 wt% MXene-TiO_2 nanocomposite showed significantly better electrochemical performance, with an electrochemical capacity of around 200 $mAhg^{-1}$ at 0.1C. Nanocomposites based on MXene-TiO_2 exhibit outstanding electrochemical performance, indicating the potential for using MXene-based nanocomposites as an anode in high-performance lithium-ion batteries.

1. Introduction

Lithium-ion batteries have been widely acknowledged as a critical component of portable electronic gadgets, driverless cars, and home energy management systems (EMSs) because of their increased energy and power densities [1–3]. All over the world, more rigorous criteria are being imposed on LIBs as floating energy storage systems with the emergence of autonomous electric cars, hybrid-electric cars, and intelligent micro-grid networks. [4,5]. Currently, graphite is being used as an anode in commercial lithium-ion batteries since its commercialization. However, due to graphite's lower working potential (vs. Li), the decomposition of organic electrolyte results in the continual formation of solid electrolyte interface (SEI) layers on graphite anodes, raising safety issues and consuming active lithium during electrochemical cycling. This results in loss of capacity and fast aging of the cells. As an alternative to graphite, Tin (Sn) and Silicon (Si) have been intensively investigated as anodes because of their higher energy densities [6]. However, significant volume changes during the electrochemical cycling, substantial irreversible capacity loss, low cyclability stability limit their use in commercial LIBs [7]. Better safety, cycling, and higher reversible capacities have prompted researchers to investigate metal oxides as anodes in high-performance lithium-ion batteries.

Due to abundance, excellent safety, eco-friendliness, and low cost, titanium dioxide (TiO_2) has been considered a promising anode material for high power density LIBs during the last decade [8–10]. Moreover, TiO_2 electrodes undergo small volume change (~5%) during the charge–discharge cycling [11]. TiO_2 comprises eight known crystal structures, rutile, anatase, brookite, TiO_2-B, TiO_2-R, TiO_2-H, TiO_2-II, TiO_2-III [12]. Over the last decades, rutile, anatase, and TiO_2-B have been rigorously explored as anode materials for lithium-ion batteries. Rutile is thermodynamically the most stable form, whereas anatase and TiO_2-B are metastable phases [13]. Additionally, due to the higher operating

* Corresponding authors.
E-mail addresses: umair.nisar@qu.edu.qa (U. Nisar), shakoor@qu.edu.qa (R.A. Shakoor).

https://doi.org/10.1016/j.apsusc.2022.152441
Received 14 November 2021; Received in revised form 24 December 2021; Accepted 3 January 2022
Available online 6 January 2022

voltage of TiO_2 (1.5 V vs. Li/Li^+), it is compatible with conventional organic-based commercial electrolytes, making it safe for high-power LIBs applications. This is because no solid electrolyte interface (SEI) forms at these working voltages, which restricts active lithium consumption and thus the continuous capacity fade [14,15]. However, TiO_2 has few intrinsic limitations, large bandgap, poor electrical conductivity, and low diffusion, which seriously prevent the practical use of TiO_2 in commercial LiBs [16,17]. This poor electrical and ionic diffusion results in high polarization [18]. Different methods to address these challenges have previously been investigated. This includes the synthesis of nanostructured TiO_2 with various morphologies, which enhances the active surface area of the particles. This leads to better ionic diffusion kinetics as the ionic transition distance within the particles decreases due to particle size reduction [19–21]. The electrochemical lithiation/de-lithiation in TiO_2 is represented by the equation (1) [22,23].

$$xLi^+ + xTiO_2 + xe^- \cdots \leftrightarrow \quad \cdots Li_xTiO_2 (0 < x < 1) \tag{1}$$

The electrochemical lithiation and de-lithiation in TiO_2 are greatly affected by its crystallinity, particle size, composition, surface energy, and polymorphism. Several approaches have been adopted to overcome the intrinsic shortcoming of TiO_2. The use of nanostructured material, carbon coatings on TiO_2, and carbon-based TiO_2 nanostructures/composites. Several nano architectures of TiO_2 have been synthesized to enhance their performance in LIBs, such as nanorods [24], nanotubes [25], and nanosheets [26]. By reducing the size of TiO_2 to nano regime, the reaction kinetics significantly improve during lithiation/de-lithiation, which results in fast charging capabilities [27]. Nevertheless, the nanomaterials tend to agglomerate, particularly during the electrochemical processes, because of their high surface activity, which may result in poor electrochemical performance [28].

Furthermore, carbon based composites have been found to increase the electronic conductivity of the electrode materials, therefore enhancing the electrochemical performance [19,29]. The mesoporous carbon/TiO_2 approach is an effective method of producing high-performance TiO_2 anodes [30]. Moreover, graphene-based TiO_2 composite anode has been reported as a positive approach to improving the performance of TiO_2 anode, which results from the unique structure of graphene with exceptionally high surface area and outstanding electrical properties [31].

More recently, MXene based anode and cathode materials have been reported, which show excellent electrochemical performance owing to exceptionally high electronic conductivities of MXene (20,000 S/cm) [32]. MXene is derived from the MAX phase (Ti_3AlC_2), a family of transition metal carbides and carbonitrides [33]. It has been observed that the electrical conductivity of demountable MXene layers was equal to multilayer graphene [34]. When employed as an anode for lithium-ion batteries, MXene nanocomposites exhibited outstanding electrochemical performance [35–38]. Ti_2C_3 is one of the most known MXenes, although few reports on its utilization in LIBs [39]. Although the usage of Ti_3C_2 as anode material in LIBs has been described, its electrochemical performance has not been promising. Moreover, the exact mechanism of intercalation/de-intercalation in MXene is not well understood [40]. However, researchers have shown that MXenes layers can be coated with several different metal oxide nanoparticles for several applications to gain the maximum advantage from their high surface due to their 2D layered structure [41,42]. However, due to the small spacings between MXene layers, it is challenging to coat the inner surface of MXene layers with these metal oxide nanoparticles [43,44]. If these MXene layers are well exfoliated and delaminated, it may be possible to thoroughly coat the inner surfaces with these nanoparticles, exploiting the advantage of the high surface area MXenes.

Herein, MXene/TiO_2 (MXene = 2, 5 and 7 wt%) anode for LIBs was developed using an in-situ process where TiO_2 nanoparticles are grown on the MXene surface. This process's advantage is that the inner surfaces of MXene layers are also well coated with TiO_2 nanoparticles due to the in-situ nucleation of TiO_2 on MXene layers. Later, during the heat treatment process, the TiO_2 particle growth due to Ostwald ripening increases the distance between MXene layers, increasing the MXene/TiO_2 anode's active surface area. For comparison purposes, nano-TiO_2 was also synthesized without any MXene. The low electrical conductivity of TiO_2 is likely to be compensated by the exceptionally high electrical conductivity of MXene. MXene/TiO_2 electrochemical performance is enhanced in terms of higher initial discharge capacity, improved rate capability, and lower cell impedance. The process employed here is quite simple, scalable without any complicated reaction steps compared to most of the published works [45–51]. Moreover, a very homogeneous TiO_2 coating is achieved both on the inner and out surfaces of MXene. Furthermore, the pseudo-capacitive character of Ti_2C_3 MXene may help to improve the electrochemical performance of MXene-TiO_2 [52].

2. Materials and methods

2.1. Synthesis of Ti_3C_2-MXene from MAX phase

1 g of the Ti_3AlC_2 powder was immersed in 20 mL of the mixed-acid solution and stirred until the Al layers' complete removal. This approach uses a lithium fluoride (LiF) salt and hydrochloric acid (HCl) to produce HF, which results in simultaneous etching and delamination of MXene. 5 mL deionized water was added in a plastic bottle, then 15 mL HCl (12 M) and 1.6 g LiF were added at 100 rpm at 35 °C, respectively. 1g Ti_3AlC_2 was slowly added to the mixture with a gradual increase in the stirring speed of 300 rpm. Under these reaction conditions, the reaction was allowed to continue for 24 h. The etched mixture was then shifted to a centrifugation tube pre-filled with DI water. The mixture was centrifuged at 3500 rpm for 10 min. Finally, the supernatant's pH was analyzed and adjusted until the solution's pH was around neutral (>6).

2.2. Synthesis of TiO_2-Ti_3C_2 MXene nanocomposites

The nano-TiO_2 was synthesized by using titanium isopropoxide (TTIP) as a precursor. Initially, 5 mL of titanium isopropoxide (TTIP) was added to 15 mL of isopropanol. Later 0.078 g of Ti_3C_2-MXene was added to this solution for 2 wt% MXene-TiO_2 and 0.197 g of Ti_3C_2-MXene was added to this solution for 5 wt% MXene-TiO_2. Moreover, 7 wt% MXene-TiO_2 was also synthesized but was discarded after initial electrochemical testing. Finally, 250 mL of deionized water was used as a hydrolysis catalyst. The PH of the solution was adjusted to around 8 by adding NH_4OH. Initially, these two solutions were mixed under vigorous stirring. TTIP hydrolysis provided a turbid solution when heated to 70 °C for almost 18–20 h (peptization). The solution volume decreased after the peptization phase, and a suspension was formed. The precipitates prepared were washed with ethanol and dried at 120 °C in a vacuum oven for 12 h to obtain amorphous MXene-TiO_2 nanocomposites. The prepared MXene-TiO_2 nanocomposite was eventually heat-treated in an argon atmosphere at 550 °C for 6 h to form a well crystalline MXene-TiO_2. Fig. 1 depicts a schematic of the synthesis process. Moreover, pure TiO_2 was also synthesized without adding MXene for comparative purposes.

2.3. Analysis and characterization

The synthesized materials' crystal structure were investigated using an X-ray diffractometer (XRD, PANalytical diffractometer) with a scan rate of 1°/min and a step size of 0.01. The synthesized materials' morphological (particle form and size) and microstructures were examined using a field emission scanning electron microscope (FE-SEM, Hitachi S-4800). To investigate the detail of structural changes, high-resolution transmission electron microscopy (HR-TEM, JEOL) was used. Particle size was analyzed from SEM images using ImageJ software. Energy-dispersive X-ray spectroscopy (EDX) was used to

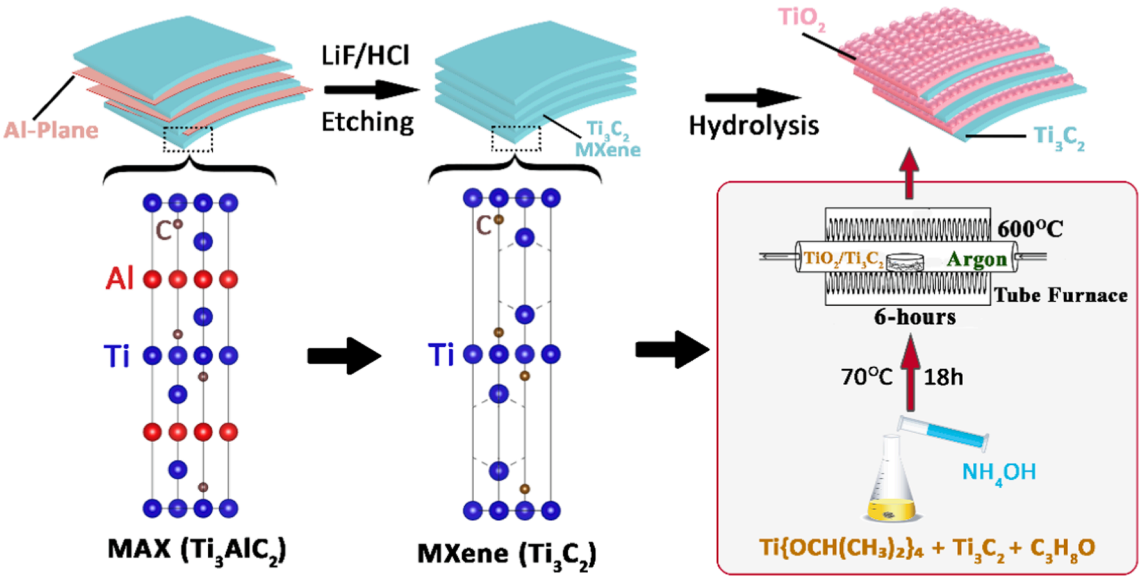

Fig. 1. Schematic representation for the synthesis of MXene-TiO_2 materials using Ti_3AlC_2 (MAX phase) as a starting material and titanium isopropoxide (TTIP) as a precursor for TiO_2.

determine the elemental composition of the synthesized materials. The thermal stability of the materials was analyzed using a TGA analyzer (Pyris 4000, PerkinElmer-USA). TGA analysis was performed from 25 °C to 700 °C at a heating rate of 10 °C/min. Lastly, Raman spectra were collected using Thermo Fisher Scientific DXR Raman Microscope with a wavelength of 532 nm to get more insights into the synthesized materials' structure.

Coin cells were used for electrochemical characterizations (CR2032). First, in n-methyl pyrrolidinone (NMP) solvent, 80 wt% active material (TiO_2 and MXene-TiO_2), 10 wt% carbon black, and 10 wt% polyvinylidene fluoride (PVDF) as a binder were evenly mixed for 6 h. Next, the slurry for later coated on copper foil (current collector) using a doctor blade. The slurry was initially dried in a conventional oven for 12 h to remove NMP. Later, the coated electrodes were dried in a vacuum oven at 120 °C for 12 h to remove moisture traces. The dried electrode sheets were punched to get the electrodes (14.5 cm in diameter). Cell fabrication was performed in an argon-filled glove box (H_2O and O_2 concentration < 0.1 ppm) using Celgard 2325 separators soaked in 125 mL of the electrolyte solution (1 M $LiPF_6$ in EC/DMC, 1:1 v/v). Lithium metal was used as a counter electrode, while TiO_2 and MXene-TiO_2 electrodes were used as anodes. To investigate the electrochemical performance of the produced materials, the cells were electrochemically cycled between 1.5 and 3.0 V using a WonAtech (WBCS 3000L) battery cycler. BioLogic (VSP, France) was used to perform cyclic voltammetry (CV) at a scan rate of 0.1 mV/s. Finally, BioLogic (VSP, France) was also used to perform electrochemical impedance spectroscopy (EIS) using a 10 mV sinusoidal signal spanning frequency ranges from 1 MHz to 10 Hz. All EIS measurements were performed at discharged at discharged states. The data collected with EIS were modeled with an electrical equivalent circuit using RelaxIS (rhd instruments, Germany) impedance analysis software.

3. Results and discussion

Fig. 2 shows the XRD spectra of TiO_2, MXene, and TiO_2-MXene (2 and 5 wt%) materials. The sharp diffraction peaks at 25.28°, 37.80°, 48.05°, 53.89°, and 55.06° are ascribed to anatase TiO_2 (JPCD: 01–078-2486). Similarly, the diffraction peaks at 6.0°, 27.44°, 34.51°, and 60.75° correspond to Ti_3C –MXene [53,54]. For the TiO_2-MXene (2 & 5 wt%), the average crystallite size of TiO_2 is calculated to be ~ 27.5 nm by the Deby-Scherrer equation. The XRD patterns of 2 & 5 wt% MXene-

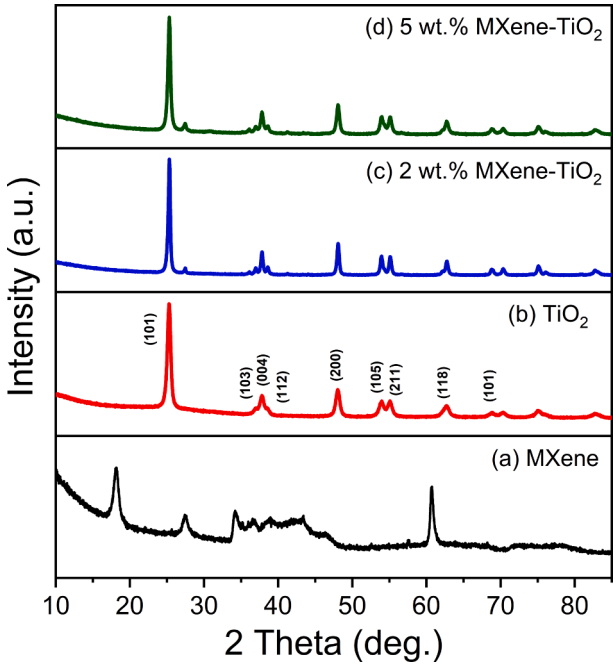

Fig. 2. XRD spectra of anatase-TiO_2, pristine MXene, and 2 & 5 wt% MXene- TiO_2.

TiO_2 exhibited the diffraction peaks of anatase-TiO_2 and Ti_3C_2-MXene, which verified the co-existence of TiO_2 and Ti_3C_2-MXene. Thus, suggesting an effective reduction from titanium isopropoxide to TiO_2 after the simultaneous hydrolysis and peptization. A comparison of the XRD spectra indicates no evidence of the presence of any impurities confirming the successful formation of phase pure 2 & 5 wt% MXene- TiO_2. Figure (S1) displays the XRD spectra of the MAX phase and Ti_3C –MXene obtained after mixed acid treatment.

To further validate the prepared materials' structure, Raman spectra of TiO_2, MXene, and 2 & 5 wt% MXene-TiO_2 were recorded as displayed in Fig. 3. Raman spectra of the synthesized materials well match with previously reported literature [55]. There are five distinct Raman scattering peaks at 144, 394, 513, and 635 cm^{-1} that correspond to the

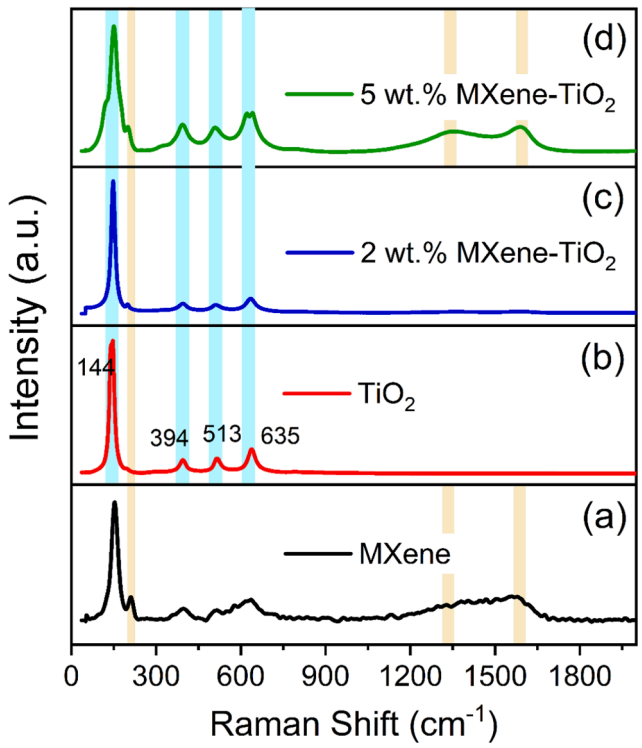

Fig. 3. Raman spectra of the (a) MXene, (b) TiO_2, (c) 2 wt% MXene-TiO_2 and (d) 5 wt% MXene-TiO_2.

anatase phase of TiO_2. The two wide spikes between 1000 and 1800 cm^{-1} were distinctive D-and G-modes of graphitic carbon of Ti_3C_2-Mxene [56,57]. The existence of graphitic carbon means that the conductive carbide layer ensures rapid charge transfer, enhancing electrochemical performance. Based on Raman spectrasand XRD results, it is confirmed that the synthesized 2 & 5 wt% MXene-TiO_2 materials are constituted of Ti_3C_2-MXene and TiO_2 anatase phase.

As shown in Fig. 4(a-b), FE-SEM micrographs display the pristine Ti_3C_2-MXene. The pristine Ti_3C_2-MXene has a layered morphology resembling an exfoliated graphite, where nanolayers are distinctly isolated. Fig. 4(c-e) displays the SEM images of 5 wt% MXene-TiO_2, which clearly shows the homogenous and complete coverage of MXene layers by TiO_2 nanoparticles (~27.5 nm). Moreover, the inner layers of MXene are also effectively coated with TiO_2 nanoparticles owing to the facile in-situ process. The insertion of TiO_2 nanoparticles into the inner surface of MXene could effectively hinder the stacking of MXene layers and expand the gap. Additionally, it was found that in 7 wt.% MXene-TiO_2 some parts of MXene were not fully coated with TiO_2 particles, which might be due to the limited amount of TiO_2 (MXene surface area > TiO_2 particles), as clearly shown in Figure S3. On the other hand, for 2 wt% MXene-TiO_2 all MXene surfaces fully coated with TiO_2 particles. However, at certain places, TiO_2 agglomerates were also seen, which suggests the insufficient MXene surfaces for these particles to cover. Therefore, based on our SEM analysis, we feel that 5 wt% MXene-TiO_2 shows the best coverage of TiO_2 particles on MXene, without the presence any bare MXene surfaces and TiO_2 agglomerates.

This would result in high TiO_2 loading on MXene surfaces, increasing energy density [58]. Two significant features can be noted in the SEM images: (1) the TiO_2 on MXene layers preserves a homogeneous morphology (size and shape); (2) Ti_3C_2-MXene retains a well laminar structure even after TiO_2 coating on the surfaces (Fig. 2 (d-e)). The SEM image for the Ti_3AlC_2 (MAX) phase, which was used as a starting material to synthesize MXene, is shown in Figure S2. It clearly shows the tight stacking of the layers without any gap.

Fig. 5 shows the Brunauer–Emmett–Teller (BET) adsorption/desorption isotherms for MXene, TiO_2, and MXene- TiO_2 (2 and 5 wt% MXene- TiO_2) materials. It can be seen from the isotherms that the 2 and 5 wt% MXene- TiO_2 materials show a much larger surface area when compared to MXene and TiO_2. 5 wt% MXene- TiO_2 shows the highest surface area of around 77.785 m^2/g compared to 2 wt% MXene-TiO_2, MXene, and TiO_2, which are around 55.687, 16.248, and 6.760 m^2/g, respectively (also listed in Table 1.). The 5 wt% MXene- TiO_2 has the

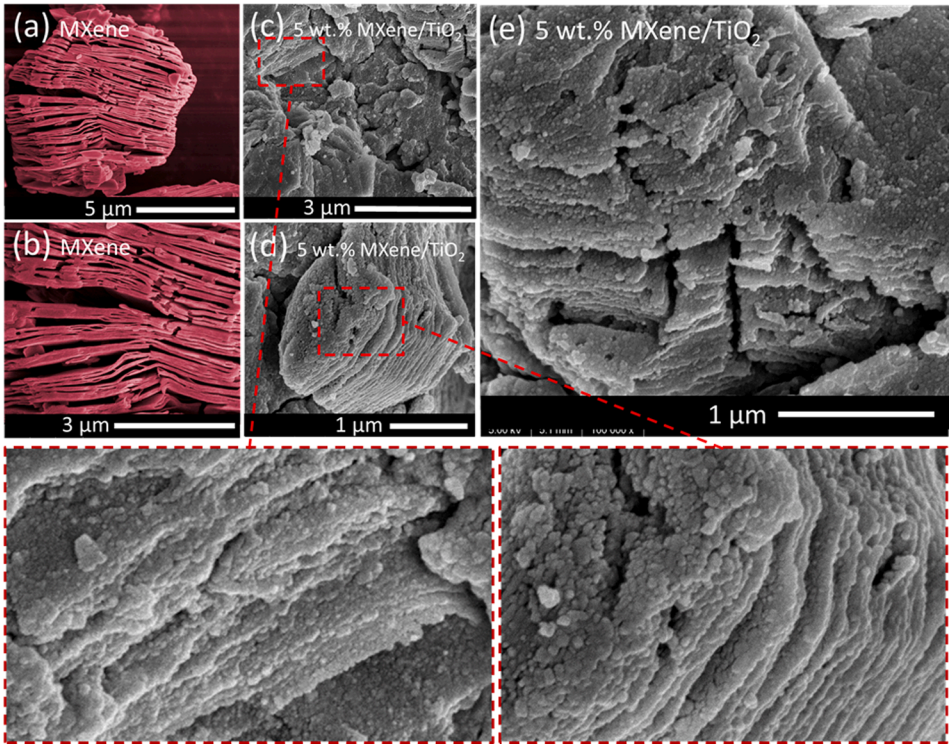

Fig. 4. SEM images for (a-b) pristine Ti_3C_2-MXene, (c-e) 5 wt% MXene-TiO_2.

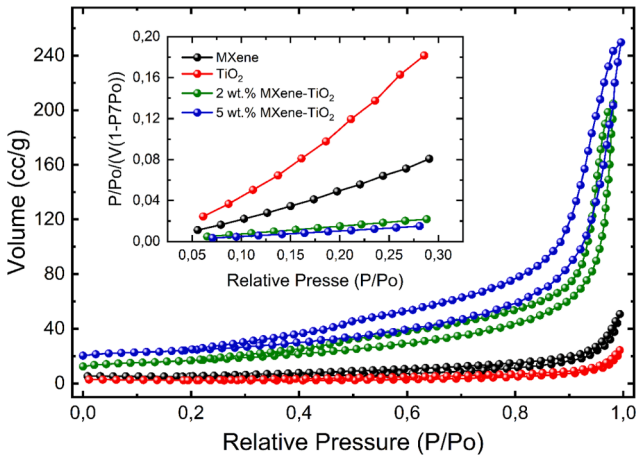

Fig. 5. BET adsorption/desorption isotherms for MXene, TiO_2, and MXene-TiO_2 materials.

Table 1
Materials and their surface area calculated from BET.

Materials	BET surface area (m^2/g)
MXene	16.248
TiO_2	6.760
2 wt% MXene-TiO_2	55.687
5 wt% MXene-TiO_2	77.785

highest surface area due to the fully covered MXene surfaces with TiO_2. On the other hand, 2 wt% MXene- TiO_2, the amount of TiO_2 is slightly more than what is required to fully cover the MXene surfaces, resulting in some TiO_2 agglomerating at certain places, which is the possible reason for the lower surface area of this material when compared to 5 wt % MXene-TiO_2.

It is also interesting to note that TiO_2 shows the lowest surface area compared to other materials. This behavior's possible reason is the agglomeration of TiO_2 nanoparticles, which decreases the surface area, a well-known phenomenon in nanomaterials. Looking at the high surface area of MXene- TiO_2 materials, it can easily be deduced that (1) introducing TiO_2 particles in between layers of MXene increased the spacing between layers exposing more surfaces to TiO_2. (2) Moreover, the coating of nano-TiO_2 on the MXene sheets increased the MXene sheets' roughness, which effectively increased the surface area of the materials, clearly supported by SEM and TEM images (Fig. 4 and Fig. 6). This morphology of MXene-TiO_2 is highly desirable for the electrochemical performance of TiO_2 since the high surface area of TiO_2 would help increase the active site for lithium intercalation/de-intercalation during electrochemical cycling resulting in enhanced performance.

The HR-TEM images and selected area electron diffraction (SAED) images of pristine MXene, 2 wt%, and 5 wt% MXene-TiO_2 nanocomposites are shown in Fig. 6. It can be seen in Fig. 6(a) that MXene displays a well-stacked layered structure. The higher resolution image in Fig. 6(b) clearly shows a single layer of MXene layer that does not show any secondary material traces. Moreover, the SAED pattern shown for MXene Fig. 6(c) confirms the hexagonal symmetry of the structure, which clearly shows that it retained the crystallinity and symmetry of the parent MAX phase Ti_2AlC [59]. On the other hand, 5 wt% MXene-TiO_2 have layers of MXene well covered with TiO_2 particles, as shown in Fig. 6(d-e). TiO_2 nanoparticles were uniformly and homogenously present on the MXene layers. HR-TEM images of 5 wt% MXene- TiO_2 (Fig. 6 (e) further clarify the homogeneous distribution of TiO_2 nanoparticles on the surface of MXene layers. Lattice fringes for TiO_2 can be seen in the HR-TEM image highlighted in white circles. HR-TEM observations demonstrate the TiO_2 nanoparticles accumulated on MXene surfaces, confirming the successful formation of MXene-TiO_2. Thus, the growth of TiO_2 nanoparticles between MXene layers increased the surface area of the MXene-TiO_2 and increased the interlayer spacings between MXene layers for Li-ion intercalation, which also resulted in additional diffusion pathways for the electrolyte. Lattice fringes indicate that TiO_2 nanoparticles have been successfully decorated on MXene. The lattice fringes corresponding to the interlayer spacing of (200) and (101) planes of TiO_2 (anatase) are observed. HR-TEM image reveals that TiO_2 nanoparticles have been incorporated onto MXene layers supporting SEM results. The SAED patterns shown for MXene-TiO_2 in Fig. 6(f) further indicate the presence of an additional phase along with MXene, which is ascribed to TiO_2 nano-particles [60,61].

Figure S4 shows the results of a TGA analysis performed between 20° and 700° C to assess the thermal stability of the produced materials. The TGA data shows that for pure Ti_3C_2-MXene, the first weight-loss stage is

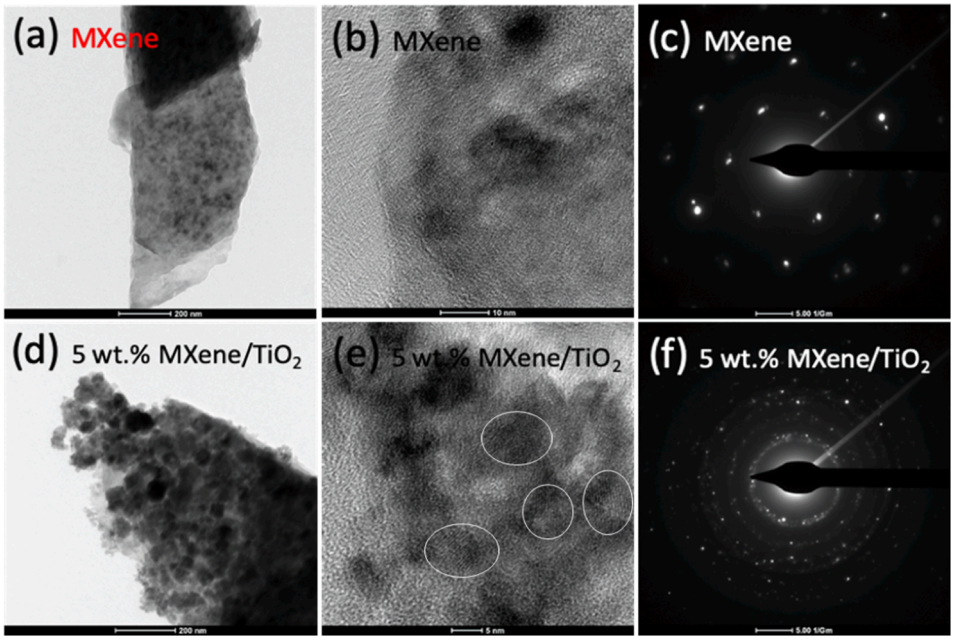

Fig. 6. HR-TEM and SAED images of (a-c) MXene, (d-f) 5 wt% MXene-TiO_2.

attributed to the loss of physically adsorbed water on the MXene surfaces (till 174.36°). The next step is the liberation of bonded water (OH) and functional groups on the surface of MXene. The third region, ~323 °C (Δm=+10%), indicates the weight gain due to oxidation of MXene.[62] In comparison, the TiO_2, 2 wt% Ti_3C_2-MXene, & 5 wt% Ti_3C_2-MXene show much stable thermogravimetric curves. The weight changes for MXene and Mxene-TiO_2 nanocomposite can be ascribed to the following two reasons: (i) TiO_2 grafted on the MXene provides thermal stability and shielding,[63] (ii) incorporation of TiO_2 reduces the heat flow, producing localized hot spots.[64] TGA results indicate that the MXene-TiO_2 nanocomposites improves the materials' structural integrity at elevated temperatures.

Fig. 7 displays the CV profiles for the 2nd cycle for TiO_2, 2 & 5 wt% MXene-TiO_2 materials at a scan rate of 0.1 mVs^{-1}. The CV profiles indicate slightly lesser polarization for 2 & 5 wt% MXene-TiO_2 material when compared to TiO_2. The inset in Fig. 7 clearly shows the oxidation peaks move to lower voltage for 2 and 5 wt% MXene-TiO_2 materials, which indicate lower polarization when compared to TiO_2 material, which would result in improved kinetics for MXene-TiO_2. Moreover, 2 & 5 wt% MXene-TiO_2 also display much higher currents during the redox activity, related to the increased electronic conductivity. On the other hand, TiO_2 shows a much lower current, reflected in its electrochemical performance compared with MXene-TiO_2 materials. Figure S4 displays the CV profiles of MXene, which corresponds to the characteristic behavior of MXene in Li-ion half-cell as previously reported [65].

The electrochemical performance of the synthesized TiO_2 and 2 & 5 wt% MXene-TiO_2 anode materials were evaluated in Li half-cells. The galvanostatic discharge/charge voltage profiles of TiO_2, 2 & 5 wt% MXene-TiO_2 at 0.1C in the voltage window of 1.5–3 V, are shown in Fig. 8. All cells show characteristic voltage plateaus at ~ 1.78 V, which can be ascribed to the oxidation/reduction of titanium (Ti^{+3}/Ti^{+4}) in TiO_2 [66]. TiO_2 and 2 & 5 wt% MXene-TiO_2 display an initial discharge capacity of around 120, 183, and 200 mAh g^{-1}. The capacity of TiO_2 after 100 cycles is only 117.8 $mAhg^{-1}$, as shown in (Fig. 8a). Contrarily, 2 & 5 wt% MXene-TiO_2 shows high initial capacity and much better capacity retention with a discharge capacity of around 165 and 180 mAh g^{-1} after 100 cycles, respectively (Fig. 8(c-d)). Moreover, 7 wt% MXene-TiO_2 was also tested for a few cycles; however, due to lower initial discharge capacity than 5 wt% MXene-TiO_2, it was not analyzed further. The reasons for the decrease in specific capacity for the 7 wt% MXene-TiO_2 can be related to an increase in the amount of inactive MXene material (as seen from Fig. S5).

The higher discharge capacity and better cycling of 2 & 5 wt% MXene-TiO_2 result from faster (de)intercalation kinetics resulting from increased electronic conductivity, the increased surface area of the MXene-TiO_2 materials, and well homogenously distributed TiO_2 on the surface of MXene layers. Moreover, this material's architecture increases the active sites for lithium (de)intercalation, resulting in much improved initial discharge capacity. On the other hand, nano-TiO_2 resulted in agglomeration, which resulted in lower initial discharge capacity and comparatively poor cycling performance. Furthermore, it can be seen that MXene-TiO_2 shows much higher coulombic efficiency (CE) when compared to TiO_2. The coulombic efficiencies were calculated based on the ratio of charge to discharge capacity. This indicated the electrochemical stability of MXene-TiO_2 as an anode.

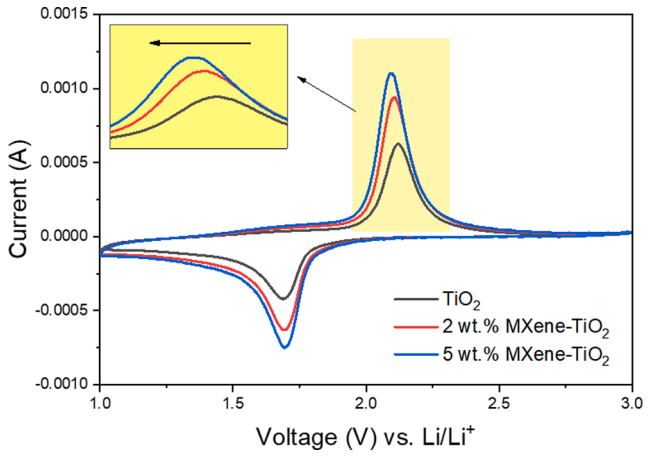

Fig. 7. Cyclic voltammetry (CV) curves for the 2nd cycle of TiO_2, 2 & 5 wt% MXene-TiO_2 at 0.1mv s^{-1}.

The rate capability of TiO_2, 2 & 5 wt% MXene-TiO_2 materials from 0.1C to 10C is shown in Fig. 9(a). TiO_2 shows the gradual capacity decay from 166 $mAhg^{-1}$(0.1C) to 20 $mAhg^{-1}$(10C). However, on the other hand, 2 & 5 wt% MXene- TiO_2 shows significantly higher capacities at all C-rates with a capacity of around 70 $mAhg^{-1}$ at 10C. Overall, 5 wt% MXene-TiO_2 shows the best rate capability compared with TiO_2 and 2 wt % MXene-TiO_2. This is due to the uniform coating of MXene layers with electrochemically active TiO_2 and the inherent high electronic conductivity of MXene. It can be seen that TiO_2 displays lower discharge capacity at all C-rates when compared with 2 & 5 wt% MXene-TiO_2. Moreover, TiO_2 also shows slightly higher polarization , resulting from the inherent poor electronic conductivity of TiO_2. On the other hand, due to the high electronic conductivity of MXene, the polarization seems to be reduced for 2 & 5 wt% MXene-TiO_2 materials. Moreover, it is interesting to see that TiO_2 anodes show lower reversible capacity when compared to MXene-TiO_2 anode, thus leading to lower coulombic efficiencies at all C-rates. The particle morphology (size and shape) of TiO_2 plays an important role in the overall electrochemical performance [67]. With nano-sized particles, they tend to agglomerate, resulting in electrode fabrication issues and poor electrochemical performance. This agglomeration problem is solved using TiO_2 grown on between the MXene layers, resulting in a homogeneous distribution of TiO_2 over MXene layers, further enhancing the loading of active material. This increases the active TiO_2 surface area, which improves the electrochemical performance.

As reported earlier [68], the aggregated particle of TiO_2 can sustain just half mole Li-ions, while well-dispersed nanoparticles can accommodate one-mole Li^+ ions per mole TiO_2. Consequently, the small interlayer spacing of MXene-TiO_2 nanocomposites thermodynamically suppresses the surface tension and aggregation between the intercalation stages[45]. This is primarily attributed to a change in the layer distance of MXene, which offers more favorable active sites for enhanced ionic mobility and reaction kinetics during lithium-ion intercalation and de-intercalation during the charging/ discharge cycling [57].

Electrochemical impedance spectroscopy (EIS) measurements were conducted to analyze the total impedance of the cells with TiO_2, 2 & 5 wt % MXene-TiO_2 materials, as illustrated in Fig. 10. The Nyquist data was fitted to a simulated equivalent circuit (inset Fig. 10) to evaluate different resistance contributions from the cell, including ohmic resistance of the cell components (R_e), SEI layer resistance (R_f), and charge-transfer resistance (R_{CT}). It can be seen from the EIS spectra that TiO_2 anode show considerably high cell impedance after figure S5 100^{th} cycles when compared to MXene-TiO_2 materials, which also reflects in the electrochemical cycling data. Moreover, the 5 wt% MXene-TiO_2 showed lowest impedance (R_{ct} = 15 Ω & R_f = 7 Ω) compared to 2 wt% MXene-TiO_2 (R_{ct} = 20 Ω & R_f = 9 Ω) and TiO_2 (R_{ct} = 35 Ω & R_f = 13 Ω) (not shown here). This is because TiO_2 is a poor electronic conductor, which results in higher cell impedance.

On the other hand, MXene has high electronic conductivity, which improves overall electronic conductivity in 2 & 5 wt% MXene-TiO_2 and decreases overall cell impedance. The high electronic conductivity of MXene results in improved redox kinetics which results in improved electrochemical performance and decreased cell impedance. It was seen that there was slight increase in impedance for 2 & 5 wt% MXene-TiO_2 after 100 cycles, whereas the TiO_2 anode indicates a marked rise in impedance after 100 cycles. The change in impedance indicates the instability of TiO_2 anode when compared with 2 & 5 wt% MXene-TiO_2

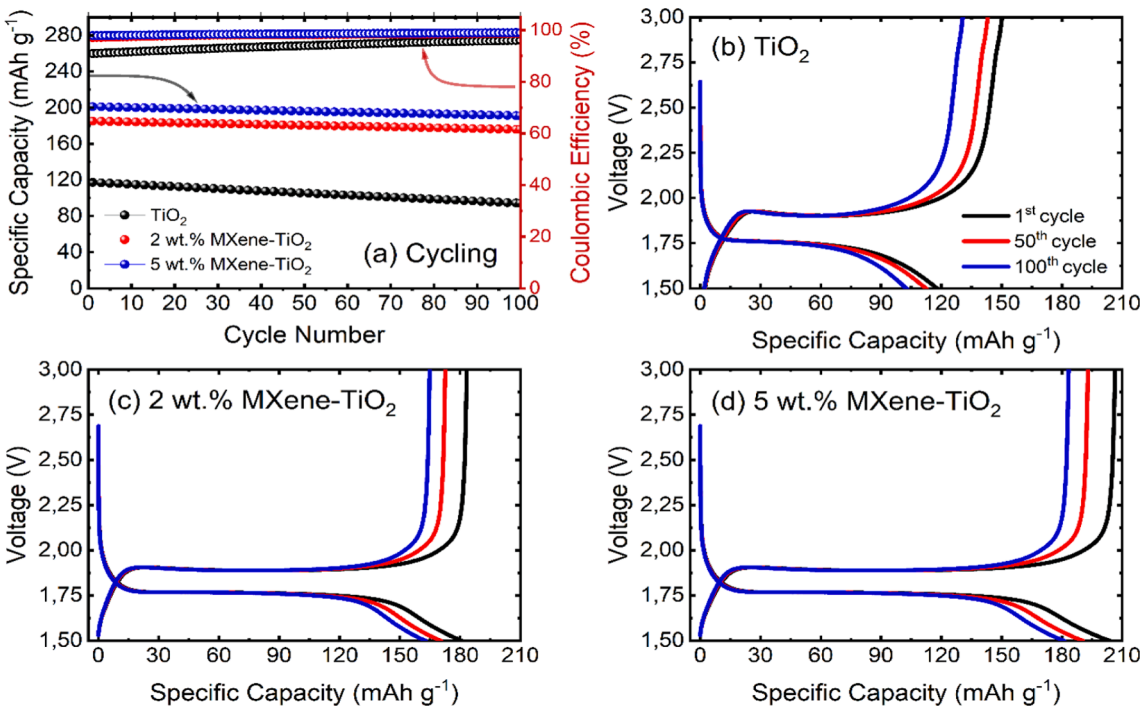

Fig. 8. A comparison of electrochemical performance of TiO_2 and MXene-TiO_2; (a) Cyclability and (b, c, d) galvanostatic charge/discharge behavior at 0.1C.

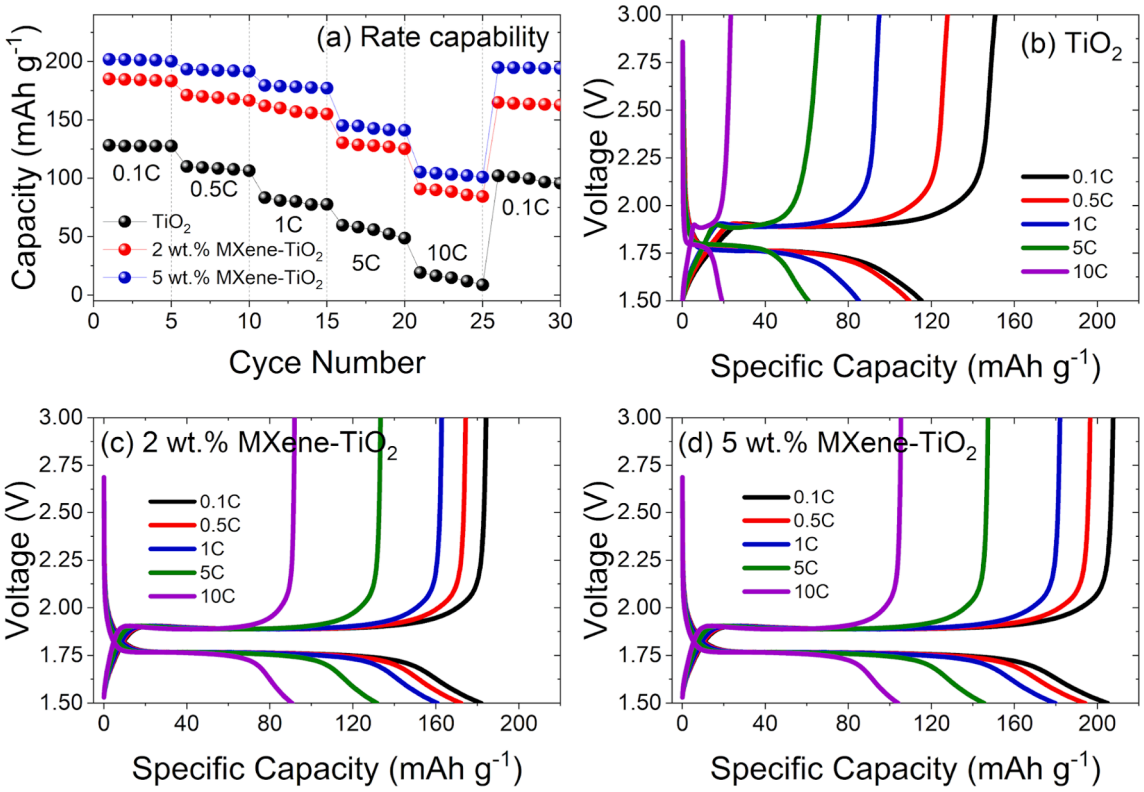

Fig. 9. (a) Rate capability of TiO_2, 2 & 5 wt% MXene-TiO_2 at room temperature, (b-c) charge/discharge behavior of the materials at progressing C-rate (b) 2 wt% MXene-TiO_2 (c) TiO_2 (d) 5 wt% MXene- TiO_2.

anodes. Thus, the lower impedance of MXene-TiO_2 indicates better kinetics for them compared to TiO_2 based cells, showing better electrochemical performance.

4. Conclusion

To conclude, firstly, the multilayered Ti_3C_2-MXene was synthesized by mixed-acid etching of Ti_3AlC_2 MAX-phase. Later, MXene layers were decorated with TiO_2 nanoparticles (~27.5 nm) through scalable

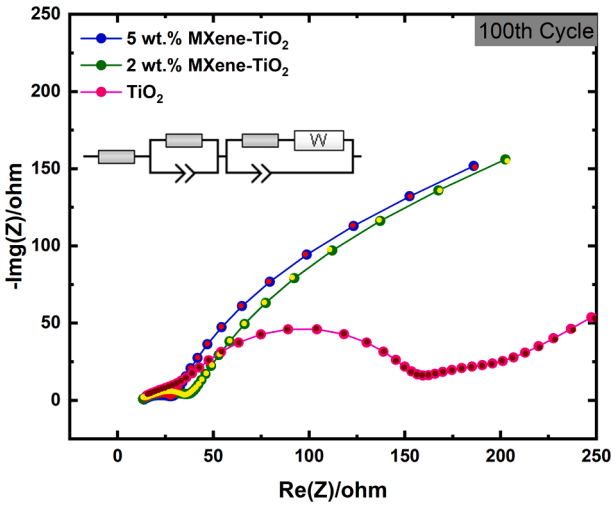

Fig. 10. EIS spectra of TiO_2, 2 & 5 wt% MXene-TiO_2 after 100th cycle.

hydrolysis of titanium isopropoxide (TTIP) to form MXene-TiO_2 material as a high-performance anode for lithium-ion batteries (LIBs). Structural analysis (XRD, SEM, HR-TEM) confirmed the presence of nano-TiO_2 on the surfaces of the MXene surface. Moreover, the TiO_2 was present even between the inner surfaces of MXene layers, which is in general not possible with ex-situ techniques. The larger surface area offered by the unique morphology guaranteed outstanding electrochemical performance of MXene-TiO_2 anodes. The 5 wt% MXene-TiO_2 materials exhibited the highest initial discharge capacity of around 200 mAh g^{-1} compared with 120 mAh g^{-1} for the TiO_2 material. Moreover, MXene-TiO_2 materials have shown much-improved rate performance compared to TiO_2 material. The reason for the superior electrochemical properties of the MXene-TiO_2 is (1) improved electronic conductivity/kinetics of MXene-TiO_2 materials, thus lowering the activation energy of lithium-ion mobility, (2) improved morphological features and surface area of MXene-TiO_2 based anodes, which provide more active sites for lithium (de)intercalation, when compared to TiO_2, (3) suppression of agglomeration of MXene-TiO_2 when compared to nano-TiO_2 based anode. If properly engineered, MXene based anodes materials have the potential for commercial applications, where MXene can act as a host material for different anode materials and simultaneously improving their structural and electronic properties.

CRediT authorship contribution statement

Hanan Abdurehman Tariq: Methodology, Investigation, Writing-Original draft preparation, Writing-Reviewing, and Editing. **Umair Nisar:** Conceptualization, Writing, Revision, and Editing. **Jeffin James Abraham:** Investigation, Writing- Original draft preparation. **Zubair Ahmad:** Writing- Reviewing and Editing. **Ramazan Kahraman:** Funding acquisition. **Siham Al-Qaradawi:** Funding acquisition, **R.A. Shakoor:** Funding acquisition, Resources, Reviewing and Editing.

Declaration of Competing Interest

The authors declare that they have no known competing financial interests or personal relationships that could have appeared to influence the work reported in this paper.

Acknowledgement

Statements made herein are solely the responsibility of the authors. Microstructural analyses (FE-SEM and HR-TEM) were accomplished at the Central Laboratory Unit (CLU), Qatar University, Doha, Qatar. Funding: This work was supported by Qatar National Research Fund (a member of the Qatar Foundation) [NPRP Grant # NPRP11S-1225-17128]; the Qatar University Internal Grant, [QUCG-CENG-20/21-2].

Data availability

The raw/processed data required to reproduce these findings cannot be shared at this time due.
to legal or ethical reasons.

Appendix A. Supplementary material

Supplementary data to this article can be found online at https://doi.org/10.1016/j.apsusc.2022.152441.

References

[1] J. Li, Next Generation Oxygen Reduction Electrocatalysts using Sustainable Materials, ProQuest Diss Theses. (2017).
[2] D.a. Deng, Li-ion batteries: Basics, progress, and challenges, Energy Sci Eng. 3 (5) (2015) 385–418, https://doi.org/10.1002/ese3.95.
[3] J. Meng, H. Guo, C. Niu, Y. Zhao, L. Xu, Q.i. Li, L. Mai, Advances in Structure and Property Optimizations of Battery Electrode Materials, Joule. 1 (3) (2017) 522–547, https://doi.org/10.1016/j.joule.2017.08.001.
[4] A.S. Aricò, P. Bruce, B. Scrosati, J.-M. Tarascon, W. van Schalkwijk, Nanostructured materials for advanced energy conversion and storage devices, Nat Mater. 4 (5) (2005) 366–377, https://doi.org/10.1038/nmat1368.
[5] N.-S. Choi, Z. Chen, S.A. Freunberger, X. Ji, Y.-K. Sun, K. Amine, G. Yushin, L. F. Nazar, J. Cho, P.G. Bruce, Challenges facing lithium batteries and electrical double-layer capacitors, Angew Chemie - Int Ed. 51 (40) (2012) 9994–10024, https://doi.org/10.1002/anie.201201429.
[6] F. Maroni, R. Raccichini, A. Birrozzi, G. Carbonari, R. Tossici, F. Croce, R. Marassi, F. Nobili, Graphene/silicon nanocomposite anode with enhanced electrochemical stability for lithium-ion battery applications, J Power Sources. 269 (2014) 873–882, https://doi.org/10.1016/j.jpowsour.2014.07.064.
[7] V. Agubra, J. Fergus, Lithium ion battery anode aging mechanisms, Materials (Basel). 6 (4) (2013) 1310–1325, https://doi.org/10.3390/ma6041310.
[8] H. Xiong, M.D. Slater, M. Balasubramanian, C.S. Johnson, T. Rajh, Amorphous TiO2 Nanotube anode for rechargeable sodium ion batteries, J Phys Chem Lett. 2 (20) (2011) 2560–2565, https://doi.org/10.1021/jz2012066.
[9] D.a. Deng, M.G. Kim, J.Y. Lee, J. Cho, Green energy storage materials: Nanostructured TiO2 and Sn-based anodes for lithium-ion batteries, Energy Environ Sci. 2 (8) (2009) 818, https://doi.org/10.1039/b823474d.
[10] C. Li, H.P. Zhang, L.J. Fu, H. Liu, Y.P. Wu, E. Rahm, R. Holze, H.Q. Wu, Cathode materials modified by surface coating for lithium ion batteries, Electrochim Acta. 51 (19) (2006) 3872–3883, https://doi.org/10.1016/j.electacta.2005.11.015.
[11] H. Liu, W. Li, D. Shen, D. Zhao, G. Wang, Graphitic Carbon Conformal Coating of Mesoporous TiO2 Hollow Spheres for High-Performance Lithium Ion Battery Anodes, J Am Chem Soc. 137 (40) (2015) 13161–13166, https://doi.org/10.1021/jacs.5b08743.
[12] L. Kavan, M. Grätzel, S.E. Gilbert, C. Klemenz, H.J. Scheel, Electrochemical and photoelectrochemical investigation of single-crystal anatase, J Am Chem Soc. 118 (28) (1996) 6716–6723, https://doi.org/10.1021/ja954172l.
[13] X. Wu, E. Holbig, G. Steinle-Neumann, Structural stability of TiO2 at high pressure in density-functional theory based calculations, J Phys Condens Matter. 22 (29) (2010) 295501, https://doi.org/10.1088/0953-8984/22/29/295501.
[14] S. Wang, B.Y. Guan, L.e. Yu, X.W.(. Lou, Rational Design of Three-Layered TiO2@Carbon@MoS2 Hierarchical Nanotubes for Enhanced Lithium Storage, Adv Mater. 29 (37) (2017) 1702724, https://doi.org/10.1002/adma.v29.3710.1002/adma.201702724.
[15] M. Pfanzelt, P. Kubiak, M. Fleischhammer, M. Wohlfahrt-Mehrens, TiO2 rutile - An alternative anode material for safe lithium-ion batteries, J Power Sources. 196 (16) (2011) 6815–6821, https://doi.org/10.1016/j.jpowsour.2010.09.109.
[16] M. Madian, A. Eychmüller, L. Giebeler, Current advances in Tio 2 -based nanostructure electrodes for high performance lithium ion batteries, Batteries. 4 (1) (2018) 7, https://doi.org/10.3390/batteries4010007.
[17] L. Dong, M. Li, L. Dong, M. Zhao, J. Feng, Y. Han, J. Deng, X. Li, D. Li, X. Sun, Hydrothermal synthesis of mixed crystal phases TiO2-reduced graphene oxide nanocomposites with small particle size for lithium ion batteries, Int J Hydrogen Energy. 39 (28) (2014) 16116–16122, https://doi.org/10.1016/j.ijhydene.2014.01.029.
[18] V. Subramanian, A. Karki, K.I. Gnanasekar, F.P. Eddy, B. Rambabu, Nanocrystalline TiO2 (anatase) for Li-ion batteries, J Power Sources. 159 (1) (2006) 186–192, https://doi.org/10.1016/j.jpowsour.2006.04.027.
[19] H.A. Tariq, J.J. Abraham, R.A. Shakoor, S. Al-Qaradawi, M.R. Abdul Karim, U. Chaudhry, Synthesis of lithium manganese oxide nanocomposites using microwave-assisted chemical precipitation technique and their performance evaluation in lithium-ion batteries, Energy Storage. 2 (6) (2020), https://doi.org/10.1002/est2.v2.610.1002/est2.202.
[20] J.-Y. Liao, D. Higgins, G. Lui, V. Chabot, X. Xiao, Z. Chen, Multifunctional TiO2-C/MnO2 core-double-shell nanowire arrays as high-performance 3D electrodes for

lithium ion batteries, Nano Lett. 13 (11) (2013) 5467–5473, https://doi.org/10.1021/nl4030159.
[21] X.u. Zhang, Z. Zhang, Z. Zhou, MXene-based materials for electrochemical energy storage, J Energy Chem. 27 (1) (2018) 73–85, https://doi.org/10.1016/j.jechem.2017.08.004.
[22] Y. Harada, K. Hoshina, H. Inagaki, N. Takami, Influence of synthesis conditions on crystal formation and electrochemical properties of TiO2(B) particles as anode materials for lithium-ion batteries, Electrochim Acta. 112 (2013) 310–317, https://doi.org/10.1016/j.electacta.2013.08.148.
[23] R. van de Krol, A. Goossens, J. Schoonman, Spatial extent of lithium intercalation in anatase TiO2, J Phys Chem B. 103 (34) (1999) 7151–7159, https://doi.org/10.1021/jp9909964.
[24] Y. Lan, X.P. Gao, H.Y. Zhu, Z.F. Zheng, T.Y. Yan, F. Wu, S.P. Ringer, D.Y. Song, Titanate nanotubes and nanorods prepared from rutile powder, Adv Funct Mater. 15 (8) (2005) 1310–1318, https://doi.org/10.1002/adfm.200400353.
[25] J. Kim, J. Cho, Rate Characteristics of Anatase TiO[sub 2] Nanotubes and Nanorods for Lithium Battery Anode Materials at Room Temperature, J Electrochem Soc. 154 (6) (2007) A542, https://doi.org/10.1149/1.2724756.
[26] J.S. Chen, L.A. Archer, X. Wen (David) Lou, SnO2 hollow structures and TiO2 nanosheets for lithium-ion batteries, J Mater Chem. 21 (27) (2011) 9912, https://doi.org/10.1039/c0jm04163g.
[27] K.-T. Kim, G. Ali, K.Y. Chung, C.S. Yoon, H. Yashiro, Y.-K. Sun, J. Lu, K. Amine, S.-T. Myung, Anatase titania nanorods as an intercalation anode material for rechargeable sodium batteries, Nano Lett. 14 (2) (2014) 416–422, https://doi.org/10.1021/nl402747x.
[28] S. Han, J. Jiang, Y. Huang, Y. Tang, J. Cao, D. Wu, X. Feng, Hierarchical TiO2-SnO2-graphene aerogels for enhanced lithium storage, Phys Chem Chem Phys. 17 (3) (2015) 1580–1584.
[29] H.A. Tariq, J.J. Abraham, A.A. Quddus, S. AlQaradawi, R. Kahraman, R. A. Shakoor, Graphene wrapped Y2O3 coated LiNi0.5Mn1.5O4 quasi-spheres as novel cathode materials for lithium-ion batteries, J Mater Res Technol. 14 (2021) 1377–1389, https://doi.org/10.1016/j.jmrt.2021.07.038.
[30] Y. Wu, Y.F. Yuan, F. Chen, M. Zhu, G.C. Cai, S.M. Yin, J.L. Yang, S.Y. Guo, TiO2 nanocrystalline-assembled mesoporous nanosphere as high-performance anode for lithium-ion batteries, Mater Lett. 240 (2019) 96–99, https://doi.org/10.1016/j.matlet.2018.12.085.
[31] Y.-H. Ding, P. Zhang, H.-M. Ren, Q. Zhuo, Z.-M. Yang, Y. Jiang, Preparation of graphene/TiO2 anode materials for lithium-ion batteries by a novel precipitation method, Mater Res Bull. 46 (12) (2011) 2403–2407, https://doi.org/10.1016/j.materresbull.2011.08.046.
[32] Y. Huang, H. Yang, Y.i. Zhang, Y. Zhang, Y. Wu, M. Tian, P. Chen, R. Trout, Y. Ma, T.-H. Wu, Y. Wu, N. Liu, A safe and fast-charging lithium-ion battery anode using MXene supported Li3VO4, J Mater Chem A. 7 (18) (2019) 11250–11256.
[33] J.-C. Lei, X.u. Zhang, Z. Zhou, Recent advances in MXene: Preparation, properties, and applications, Front Phys. 10 (3) (2015) 276–286, https://doi.org/10.1007/s11467-015-0493-x.
[34] Q. Tang, Z. Zhou, Graphene-analogous low-dimensional materials, Prog Mater Sci. 58 (8) (2013) 1244–1315, https://doi.org/10.1016/j.pmatsci.2013.04.003.
[35] X. Hui, R. Zhao, P. Zhang, C. Li, C. Wang, L. Yin, Low-Temperature Reduction Strategy Synthesized Si/Ti3C2 MXene Composite Anodes for High-Performance Li-Ion Batteries, Adv Energy Mater. 9 (33) (2019) 1901065, https://doi.org/10.1002/aenm.v9.3310.1002/aenm.201901065.
[36] R. Zhang, Z. Xue, J. Qin, M. Sawangphruk, X. Zhang, R. Liu, NiCo-LDH/Ti3C2 MXene hybrid materials for lithium ion battery with high-rate capability and long cycle life, J Energy Chem. 50 (2020) 143–153, https://doi.org/10.1016/j.jechem.2020.03.018.
[37] Y. Tian, Y. An, C. Wei, Y. Tao, Y. Zhang, H. Jiang, L. Tan, J. Feng, Y. Qian, Stable and dendrite-free lithium metal anodes enabled by carbon paper incorporated with ultrafine lithiophilic TiO2 derived from MXene and carbon dioxide. *Chem*, Eng J. 406 (2021) 126836, https://doi.org/10.1016/j.cej.2020.126836.
[38] J. Li, L.u. Han, Y. Li, J. Li, G. Zhu, X. Zhang, T. Lu, L. Pan, MXene-decorated SnS2/Sn3S4 hybrid as anode material for high-rate lithium-ion batteries. *Chem*, Eng J. 380 (2020) 122590, https://doi.org/10.1016/j.cej.2019.122590.
[39] D. Er, J. Li, M. Naguib, Y. Gogotsi, V.B. Shenoy, Ti3C2 MXene as a high capacity electrode material for metal (Li, Na, K, Ca) ion batteries, ACS Appl Mater Interfaces. 6 (14) (2014) 11173–11179, https://doi.org/10.1021/am501144q.
[40] X. Mu, D. Wang, F. Du, G. Chen, C. Wang, Y. Wei, Y. Gogotsi, Y.u. Gao, Y. Dall'Agnese, Revealing the Pseudo-Intercalation Charge Storage Mechanism of MXenes in Acidic Electrolyte, Adv Funct Mater. 29 (29) (2019) 1902953, https://doi.org/10.1002/adfm.v29.2910.1002/adfm.201902953.
[41] D. Xiong, X. Li, Z. Bai, S. Lu, Recent Advances in Layered Ti3C2Tx MXene for Electrochemical Energy Storage, Small. 14 (17) (2018) 1703419, https://doi.org/10.1002/smll.v14.1710.1002/smll.201703419.
[42] L. Wan, D.H.C. Chua, H. Sun, L. Chen, K. Wang, T. Lu, L. Pan, Construction of two-dimensional bimetal (Fe-Ti) oxide/carbon/MXene architecture from titanium carbide MXene for ultrahigh-rate lithium-ion storage, J Colloid Interface Sci. 588 (2021) 147–156, https://doi.org/10.1016/j.jcis.2020.12.071.
[43] Y. Wang, Y. Li, Z. Qiu, X. Wu, P. Zhou, T. Zhou, J. Zhao, Z. Miao, J. Zhou, S. Zhuo, Fe3O4@Ti3C2 MXene hybrids with ultrahigh volumetric capacity as an anode material for lithium-ion batteries, J Mater Chem A. 6 (24) (2018) 11189–11197.
[44] S. Sun, Z. Xie, Y. Yan, S. Wu, Hybrid energy storage mechanisms for sulfur-decorated Ti3C2 MXene anode material for high-rate and long-life sodium-ion batteries, Chem Eng J. 366 (2019) 460–467, https://doi.org/10.1016/j.cej.2019.01.185.
[45] L.i. Li, G. Jiang, C. An, Z. Xie, Y. Wang, L. Jiao, H. Yuan, Hierarchical Ti3C2@TiO2 MXene hybrids with tunable interlayer distance for highly durable lithium-ion batteries, Nanoscale. 12 (18) (2020) 10369–10379.
[46] C. Li, Z. Xue, J. Qin, M. Sawangphruk, P. Yu, X. Zhang, R. Liu, Synthesis of nickel hydroxide/delaminated-Ti3C2 MXene nanosheets as promising anode material for high performance lithium ion battery, J Alloys Compd. 842 (2020) 155812, https://doi.org/10.1016/j.jallcom.2020.155812.
[47] U. Alli, K. McCarthy, I.-A. Baragau, N.P. Power, D.J. Morgan, S. Dunn, S. Killian, T. Kennedy, S. Kellici, In-situ continuous hydrothermal synthesis of TiO2 nanoparticles on conductive N-doped MXene nanosheets for binder-free Li-ion battery anodes, Chem Eng J. 430 (2022) 132976, https://doi.org/10.1016/j.cej.2021.132976.
[48] S. Xiao, X. Zhang, J. Zhang, S. Wu, J. Wang, J.S. Chen, T. Li, Enhancing the lithium storage capabilities of TiO2 nanoparticles using delaminated MXene supports, Ceram Int. 44 (15) (2018) 17660–17666, https://doi.org/10.1016/j.ceramint.2018.06.228.
[49] L. Sun, J. Xie, L. Zhang, R. Jiang, J. Wu, L. Fan, R. Shao, Z. Chen, Z. Jin, 2D black TiO2-x nanoplate-decorated Ti3C2 MXene hybrids for ultrafast and elevated stable lithium storage, FlatChem. 20 (2020) 100152, https://doi.org/10.1016/j.flatc.2020.100152.
[50] C. Du, J. Wu, P. Yang, S. Li, J. Xu, K. Song, Embedding S@TiO2 nanospheres into MXene layers as high rate cyclability cathodes for lithium-sulfur batteries, Electrochim Acta. 295 (2019) 1067–1074, https://doi.org/10.1016/j.electacta.2018.11.143.
[51] Z. Dai, J. Cao, F. Song, D. Zhang, J. Qin, X. Zhang, Architecting Nb-TiO2−x/(Ti0.9Nb0.1)3C2Tx MXene Nanohybrid Anode for High-Performance Lithium-Ion Batteries, Adv Mater Interfaces (2021) 2101658, https://doi.org/10.1002/admi.202101658.
[52] J. Come, Y.u. Xie, M. Naguib, S. Jesse, S.V. Kalinin, Y. Gogotsi, P.R.C. Kent, N. Balke, Nanoscale Elastic Changes in 2D Ti3C2Tx (MXene) Pseudocapacitive Electrodes, Adv Energy Mater. 6 (9) (2016) 1502290, https://doi.org/10.1002/aenm.201502290.
[53] X. Xie, Y. Xue, L.i. Li, S. Chen, Y. Nie, W. Ding, Z. Wei, Surface Al leached Ti3AlC2as a substitute for carbon for use as a catalyst support in a harsh corrosive electrochemical system, Nanoscale. 6 (19) (2014) 11035–11040.
[54] O. Mashtalir, M.R. Lukatskaya, A.I. Kolesnikov, E. Raymundo-Piñero, M. Naguib, M.W. Barsoum, Y. Gogotsi, The effect of hydrazine intercalation on the structure and capacitance of 2D titanium carbide (MXene), Nanoscale. 8 (17) (2016) 9128–9133.
[55] M. Naguib, O. Mashtalir, M.R. Lukatskaya, B. Dyatkin, C. Zhang, V. Presser, Y. Gogotsi, M.W. Barsoum, One-step synthesis of nanocrystalline transition metal oxides on thin sheets of disordered graphitic carbon by oxidation of MXenes, Chem Commun. 50 (56) (2014) 7420–7423.
[56] T. Ohsaka, F. Izumi, Y. Fujiki, Raman spectrum of anatase, TiO2, J Raman Spectrosc. 7 (6) (1978) 321–324, https://doi.org/10.1002/jrs.1250070606.
[57] M. Hu, Z. Li, T. Hu, S. Zhu, C. Zhang, X. Wang, High-Capacitance Mechanism for Ti3C2Tx MXene by in Situ Electrochemical Raman Spectroscopy Investigation, ACS Nano 10 (12) (2016) 11344–11350, https://doi.org/10.1021/acsnano.6b0659710.1021/acsnano.6b06597.s001.
[58] H. Zhang, P. Zhang, W. Zheng, W. Tian, J. Chen, Y. Zhang, ZhengMing Sun, 3D d-Ti3C2 xerogel framework decorated with core-shell SnO2@C for high-performance lithium-ion batteries, Electrochim Acta. 285 (2018) 94–102, https://doi.org/10.1016/j.electacta.2018.07.198.
[59] R. Li, L. Zhang, L. Shi, P. Wang, MXene Ti 3 C 2: An Effective 2D Light-to-Heat Conversion Material, ACS Nano 11 (4) (2017) 3752–3759, https://doi.org/10.1021/acsnano.6b08415.
[60] B. Ahmed, D.H. Anjum, M.N. Hedhili, Y. Gogotsi, H.N. Alshareef, H 2 O 2 assisted room temperature oxidation of Ti 2 C MXene for Li-ion battery anodes, Nanoscale. 8 (14) (2016) 7580–7587, https://doi.org/10.1039/C6NR00002A.
[61] S. Topcu, G. Jodhani, P.I. Gouma, Optimized Nanostructured TiO2 Photocatalysts, Front Mater. 3 (2016), https://doi.org/10.3389/fmats.2016.00035.
[62] Y. Sun, Y. Sun, X. Meng, Y.u. Gao, Y. Dall'Agnese, G. Chen, C. Dall'Agnese, X.-F. Wang, Eosin Y-sensitized partially oxidized Ti 3 C 2 MXene for photocatalytic hydrogen evolution, Catal Sci Technol. 9 (2) (2019) 310–315.
[63] L.A. Ardila Rodriguez, D.N. Travessa, Core/Shell Structure of TiO2-Coated MWCNTs for Thermal Protection for High-Temperature Processing of Metal Matrix Composites. *Adv*, Mater Sci Eng. 2018 (2018) 1–11, https://doi.org/10.1155/2018/7026141.
[64] Y. Sun, Z. Xu, Y. Zhuang, G. Liu, W. Jin, G. Liu, W. Jing, Tunable dextran retention of MXene-TiO 2 mesoporous membranes by adjusting the 2D MXene content, 2D Mater. 5 (4) (2018) 045003, https://doi.org/10.1088/2053-1583/aad01e.
[65] C.-H. Wang, N. Kurra, M. Alhabeb, J.-K. Chang, H.N. Alshareef, Y. Gogotsi, Titanium Carbide (MXene) as a Current Collector for Lithium-Ion Batteries, ACS Omega 3 (10) (2018) 12489–12494, https://doi.org/10.1021/acsomega.8b02032.
[66] J. Wang, Y. Zhou, Y. Hu, R. O'Hayre, Z. Shao, Facile synthesis of nanocrystalline TiO2 mesoporous microspheres for lithium-ion batteries, J Phys Chem C. 115 (5) (2011) 2529–2536, https://doi.org/10.1021/jp1087509.
[67] B.-L. He, B. Dong, H.-L. Li, Preparation and electrochemical properties of Ag-modified TiO2 nanotube anode material for lithium-ion battery, Electrochem commun. 9 (3) (2007) 425–430, https://doi.org/10.1016/j.elecom.2006.10.008.
[68] M. Wagemaker, W.J.H. Borghols, F.M. Mulder, Large impact of particle size on insertion reactions. A case for anatase LixTiO2, J Am Chem Soc. 129 (14) (2007) 4323–4327, https://doi.org/10.1021/ja067733p.